Published in final edited form as:

ACS Appl Bio Mater. 2021 September 20; 4(9): 7025–7033. doi:10.1021/acsabm.1c00677.

Photodynamic Activity of Graphene Oxide/Polyaniline/Manganese Oxide Ternary Composites toward Both Gram-Positive and Gram-Negative Bacteria

Gustavo Chata,
Department of Chemistry and Biochemistry, University of California, Santa Cruz, California 95064, United States

Forrest Nichols,
Department of Chemistry and Biochemistry, University of California, Santa Cruz, California 95064, United States

Rene Mercado,
Department of Chemistry and Biochemistry, University of California, Santa Cruz, California 95064, United States

Tufa Assafa,
Department of Chemistry and Biochemistry, University of California, Santa Cruz, California 95064, United States

Glenn L. Millhauser,
Department of Chemistry and Biochemistry, University of California, Santa Cruz, California 95064, United States;

Chad Saltikov,
Department of Microbiology and Environmental Toxicology, University of California, Santa Cruz, California 95064, United States

Shaowei Chen
Department of Chemistry and Biochemistry, University of California, Santa Cruz, California 95064, United States;

Abstract

Corresponding Author: **Shaowei Chen** – Department of Chemistry and Biochemistry, University of California, Santa Cruz, California 95064, United States; shaowei@ucsc.edu.

Author Contributions

The manuscript was written through contributions of all authors. All authors have given approval to the final version of the manuscript.

Supporting Information

The Supporting Information is available free of charge at https://pubs.acs.org/doi/10.1021/acsabm.1c00677.

Additional experimental data of the sample series, including comparison of Mn contents from XPS and ICP-OES measurements, photograph of the experimental setup for the photodynamic experiments, high-resolution TEM images, XRD patterns, XPS survey spectra, SEM images and corresponding EDS spectra, high-resolution C 1s spectra, growth curves of *S. epidermidis* in the dark, and CFU experiment under 365 nm photoirradiation (PDF)

Complete contact information is available at: https://pubs.acs.org/10.1021/acsabm.1c00677

The authors declare no competing financial interest.

Graphene derivatives have been attracting extensive interest as effective antimicrobial agents. In the present study, ternary nanocomposites are prepared based on graphene oxide quantum dots (GOQD), polyaniline (PANI), and manganese oxides. Because of the hydrophilic GOQD and PANI, the resulting GPM nanocomposites are readily dispersible in water and upon photoirradiation at 365 nm exhibit antimicrobial activity toward both Gram-negative *Escherichia coli* (*E. coli*) and Gram-positive *Staphylococcus epidermidis* (*S. epidermidis*). Notably, the nanocomposite with a high Mn^{2+} and Mn^{4+} content is found to be far more active than that with a predominant Mn^{3+} component, although both samples feature a similar elemental composition and average Mn valence state. The bactericidal activity is largely ascribed to the photocatalytic production of hydroxy radicals and photogenerated holes; both are known to exert oxidative stress on bacterial cells. Further antimicrobial contributions may arise from the strong affinity of the nanocomposites to the cell surfaces. These results suggest that the metal valence state may be a critical parameter in the design and engineering of high-performance antimicrobial agents based on metal oxide nanocomposites.

Graphical Abstract

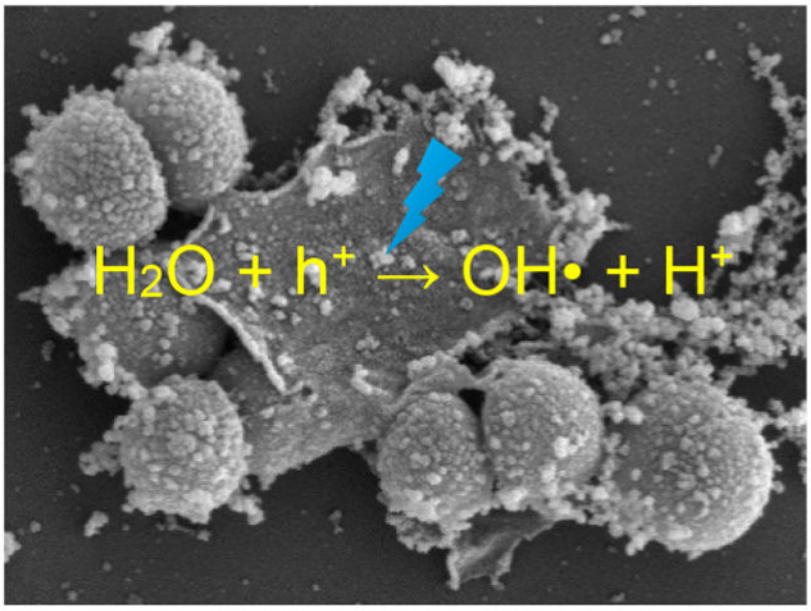

Keywords

ternary composite; manganese oxide; antimicrobial; photodynamic; hydroxy radical; hole

INTRODUCTION

The continuous widespread application of antibiotics to Gram-negative and Gram-positive bacteria has led to the evolution of enzymatic resistance.[1] Thus, it is of both fundamental and technological significance to develop alternative antimicrobial agents that can combat antibiotic resistance. The bactericidal activity of graphene-based nanocomposites has been attracting extensive interest because of their known combination of actions, such as

oxidative stress induction, protein dysfunction, membrane damage, and transcriptional arrest.[2] For instance, it has been found that graphene oxide quantum dots (GOQDs), prepared by oxidative exfoliation of carbon fibers, exhibited apparent antimicrobial activity against *Staphylococcus epidermidis* (*S. epidermidis*), and the cytotoxicity was markedly diminished when the GOQDs were chemically reduced by $NaBH_4$. This was ascribed to effective removal by $NaBH_4$ reduction of redox-active phenanthroline-like moieties that interacted with the electron-transport chain of the bacterial cells and diminished production of hydroxyl radicals that were potent bactericidal agents after chemical reduction, as a result of increased conjugation within the carbon skeletons.[3] The antimicrobial activity can be enhanced by the formation of nanocomposites with metal oxide nanoparticles, such as ZnO, TiO_2, Cu_2O, Fe_xO_y, and Ag_2O, where the high photocatalytic activity of the latter can be exploited for the enhanced production of reactive oxygen species (ROS).[4,5] In a previous study,[6] photoactive ZnO/GQD nanocomposites were prepared by a facile hydrothermal method, and the bactericidal activity toward Gram-negative *Escherichia coli* (*E. coli*) was found to be markedly improved under UV photoirradiation, as compared to that in ambient light. This was accounted for by the photoillumination that facilitated the generation of ROS with minor contributions from membrane damage, as manifested in electron paramagnetic resonance (EPR) and fluorescence microscopic measurements. The antimicrobial activity can be further enhanced by the formation of a ternary composite with a cationic polymer due to enhanced electrostatic interactions with bacterial cell membranes.[7] Similarly, Cao et al.[8] demonstrated an enhanced photodynamic antibacterial activity of TiO_2–graphene nanosheet nanocomposites, which featured a tunable band gap as a function of reduced graphene oxide (rGO) deposition. In another study,[9] three-dimensional networks of rGO nanosheets hybridized with vertically aligned CuO nanowires were prepared by a combined thermal oxidation/electrophoretic deposition method and exhibited apparent antimicrobial activity toward *E. coli*. This was ascribed to photoinduced electron injection from CuO into rGO, where the resulting excess electrons on the rGO functional groups led to the ready production of ROS and eventual bacterial cell death.

Notably, manganese oxides have also emerged as attractive photocatalysts, in particular, for the degradation of organic pollutants, due to their good performance, high natural abundance, and minimal impact on the environment.[10] Interestingly, the photocatalytic activity has been found to vary with the Mn valence state. For instance, the activity toward oxone activation exhibited a trend of $Mn_2O_3 > MnO > Mn_3O_4 > MnO_2$,[11] whereas the efficacy of the photocatalytic degradation of alizarin yellow varied in the order of $MnO_2 > Mn_3O_4 > MnOOH$. A higher band gap energy was correlated with enhanced photocatalytic activity, likely due to an adjustment in the band structure that facilitated ROS production.[12] Notably, studies of manganese oxides as photoactive bactericidal agents have been scarce.[13–15] Thus, one immediate question arises. Will the Mn valence state impact the antimicrobial activity? This is the primary motivation of the present study.

Herein, ternary nanocomposites were prepared whereby manganese oxides (MnO_x) were deposited onto GOQD/polyaniline (PANI) hybrids. The resulting GPM nanocomposites were found to contain a consistent content of Mn with an average valence state of ca. 2.8. Notably, the sample that featured a substantial Mn^{2+} and Mn^{4+} component exhibited markedly enhanced antimicrobial activity under 365 nm photoirradiation toward both Gram-

negative *E. coli* and Gram-positive *S. epidermidis*, as compared to the sample with a dominant Mn^{3+} component. This was ascribed to the different photocatalytic activity in ROS production, as manifested in photoluminescence measurements where the former sample was found to exhibit much quenched emission, suggesting enhanced efficiency of the separation of photogenerated electron–hole pairs. EPR measurements showed that the bactericidal activity was primarily due to hydroxy radicals (HO•) and photogenerated holes (h^+). These results indicate that effective antimicrobial agents can be obtained with a deliberate variation of the valence state of the photoactive species.

EXPERIMENTAL SECTION

Chemicals.

Aniline (99.8%), ammonium persulfate (APS, 99.8%), potassium permanganate ($KMnO_4$, 99.0%), polyvinylpyrrolidone (PVP, MW 3500), ethylenediaminetetraacetic acid disodium salt dihydrate (EDTA-2Na, 99.0%), *tert*-butanol (TBA, 99.5%), 5,5-dimethyl-1-pyrroline *N*-oxide (DMPO, ≥97%), and glutaraldehyde (25.0%) were all purchased from ACROS or Sigma-Aldrich and used as received. Water was purified with a Barnstead Nanopure Water System (18.3 MΩ cm).

Sample Preparation.

GOQD.—The synthesis of GOQD has been detailed previously.[3] In brief, pitch carbon fiber (1 g) was immersed into a mixture of concentrated HNO_3 (40 mL) and H_2SO_4 (60 mL) in a round-bottom flask. After 2 h of sonication, the carbon fibers were refluxed at 120 °C for 24 h. Once the solution was cooled down to room temperature, the pH was adjusted to pH 7 with NaOH and the solution was left overnight to allow for salts to precipitate out of solution. The supernatant, which contained water-soluble GOQD, was collected and transferred to a cellulose dialysis bag, which was placed in Nanopure water for several days to afford purified GOQD.

Manganese Oxides.—Two manganese oxides (Mn_xO_y) were prepared by adopting different literature protocols.[16–18] In the first method,[16] 90 mg of $KMnO_4$ and 27 mg of PVP were dissolved in 30 mL of water under stirring for 10 min, which formed a homogeneous purple solution. The solution was transferred to a Teflon-lined steel autoclave, sealed, and heated at 170 °C for 12 h. The precipitates were then collected by centrifugation, washed with water and ethanol several times, and dried in a vacuum oven, affording solid powers that contained a mixture of MnO and MnO_2.

MnOOH was prepared by adopting a different procedure.[17] In brief, 3 mL of absolute ethanol was added into 47 mL of an aqueous solution of $KMnO_4$ (0.1 M) under magnetic stirring at room temperature. The mixture was then transferred into a Teflon-lined steel autoclave, sealed, and heated at 140 °C for 24 h. The purified precipitates were dominantly MnOOH, with a small fraction of MnO.

GOQD/PANI/Mn_xO_y Composites.—A 25 mg amount of the GOQD prepared above was dissolved in 100 mL of Nanopure water under sonication for 1 h, into which was slowly

added 12 mL of aniline, followed by a solution containing 12.25 mg of APS in 10 mL of 5.4 mM HCl, and after reaction in an ice bath for 10 min, a solution containing 25 mg of the manganese oxides prepared above dispersed in hydrochloric acid (1 M, 50 mL). The reaction was allowed under stirring for 12 h, and the solution was dialyzed in Nanopure water for 3 days, affording purified GOQD/PANI/Mn_xO_y composites which are denoted as GPM-1 and GPM-2. A control sample was also prepared in the same manner but without the addition of manganese oxides and referred to as GP.

Characterization.

The morphology of the samples was characterized by transmission electron microscopy (TEM, Phillips CM 300 at 300 kV) and scanning electron microscopy (SEM, FEI Quanta field emission microscope) measurements. UV–vis absorption spectra were acquired with a PerkinElmer Lambda 35 UV–vis spectrophotometer, and photoluminescence measurements were conducted with a PTI fluorospectrophotometer. X-ray photoelectron spectra (XPS) were recorded with a PHI 5400/XPS instrument equipped with an Al Kα source operated at 350 W and 10^{-9} Torr. X-ray diffraction (XRD) studies were conducted with a Rigaku D/MAX-2200 diffractometer with Cu Kα radiation (λ = 1.540 Å). Inductively coupled plasma-optical emission spectroscopy (ICP-OES) measurements were carried out with a PerkinElmer Optima Instrument. Energy-dispersive X-ray spectroscopy (EDS) measurements were performed with an Apreo 2 SEM.

Antimicrobial Assay.

E. coli and *S. epidermidis* cells were grown in Luria–Bertani (LB) agar in a 37 °C incubator. A single colony was selected and used to inoculate 3 mL of LB broth and allowed to shake at 37 °C for 18 h. The resulting liquid was centrifuged at 5000 rpm for 5 min and resuspended in Nanopure water to an optical density (OD) of 0.1 at 600 nm. To determine the minimum inhibition concentration (MIC), a 96-well plate was used to conduct a kinetic cell growth experiment in the dark at 37 °C. Each well was filled to a total volume of 200 μL with 30 μL of sterile LB, 10 μL of bacterial solution, and varied volumes of the nanocomposite samples prepared above. Sterile Nanopure water was used to bring the total volume in each well to 200 μL. Upon inoculation, the 96-well plate was placed in a Molecular Device VERSA max microplate reader, where the OD was measured at 600 nm every 90 s with intermittent shaking between each reading over a 24 h incubation period. In photodynamic antibacterial assessments, 200 μL of *E. coli* or *S. epidermidis* (OD = 0.1) was transferred to a 1.5 mL plastic microcentrifuge tube, into which 600 μL of the nanocomposite samples (1 mg mL^{-1}) was added along with 200 μL of sterilized Nanopure water. The centrifuge tubes containing the bacterial cells and composites were irradiated with a UV lamp (100 W, 1000–1500 lm with a peak emission at 365 nm, Dongguan Hongke Lighting Co, China) (Figure S1). After irradiation, the cells in each centrifuge tube were diluted 100-fold for each respective time point. From the diluted solution, 10 μL was spread plated on LB agar plates using sterile glass beads. The agar plates were incubated at 37 °C, and the number of bacterial colony forming units (CFU) was counted by visual inspection. The percent cell survival was calculated by normalizing the CFUs to the value without any photoirradiation.

EPR Measurements.

In EPR measurements, 63 μL of the nanocomposites prepared above (1 mg mL^{-1}) was mixed with 7 μL of 1 mol L^{-1} DMPO, with a mixture of Nanopure H_2O and DMPO as a control. The solution was then added to a capillary tube which was inserted into a quartz EPR tube (Wilmad, 4 mm outer diameter). The tube was centered in the cavity resonator for data collection. Spectra were recorded at room temperature with a Bruker EMX EPR spectrometer operating at the X-band frequency (~9.3 GHz) using an ER 4122SHQE resonator (Bruker). The samples were subsequently irradiated for 10 min with 365 nm UV light prior to the collection of EPR spectra.

RESULTS AND DISCUSSION

The GPM samples were prepared via a two-step procedure: (a) the preparation of manganese oxide compounds by hydrothermal reduction of $KMnO_4$ and separately GOQD/PANI hybrids by polymerization of aniline onto the GOQD surface; (b) mixing the two materials to afford ternary GPM composites. The sample structure was first characterized by SEM and TEM measurements. From the SEM images in Figure 1a and 1b, one can see that the GPM samples consisted mostly of particles of 100–300 nm in diameter. In TEM measurements (Figure 1c and 1d), these particles exhibited a flaky, porous network structure, and no well-defined lattice fringes could be resolved in high-resolution measurements (Figure S2), suggesting the formation of an amorphous structure, consistent with results from XRD measurements (Figure S3). Note that the GPM composites are readily dispersible in water, mostly because of the combined contributions of the hydrophilic GOQD and PANI support. In UV–vis measurements (Figure 1e), both the GP and the GPM samples exhibited three absorption peaks at 232, 260, and 284 nm due to the π–π* transitions of the sp^2 carbon in GOQD.[19–21] The GPM samples also contain a peak at 270 nm, characteristic of quinone absorption, which likely arose from the oxidation of PANI by manganese oxides. In photoluminescence emission measurements, the GPM and GP samples all showed a sole emission peak around 485 nm, most likely due to the σ*–n electronic transition in GOQD and near band-edge emission from the emeraldine base form of PANI.[22,23] Notably, one can see that within the sample series, the GPM-1 nanocomposites exhibited the lowest (normalized) emission intensity, suggesting the most efficient separation of the photogenerated electron–hole pairs, which is conducive for ROS production and photodynamic activity, as detailed below.

The elemental compositions and valence states of the sample series were then examined by XPS measurements. From the survey spectra (Figure S4), the C 1s, N 1s, O 1s, and Mn 3p electrons can be readily identified at ca. 284, 400, 530, and 640 eV, respectively, in good agreement with the formation of ternary composites. On the basis of the integrated peak areas, the elemental compositions were then estimated, which were consistent among the sample series, including 60–70 atom % C, slightly under 6 atom % N, 23–30 atom % O, and 0.4 atom % Mn (Table 1). Consistent results were obtained for the Mn contents by ICP-OES measurements (Table S1) and EDS measurements (Figure S5 and S6). Because of the low Mn contents, no obvious diffraction patterns were observed in XRD measurements for the manganese species (Figure S3).

Figure 2a shows the high-resolution scans of the N 1s electrons in GP, GPM-1, and GPM-2. One can see that for all samples, deconvolution yielded three major components that can be ascribed to quinoid (398.4 eV), benzenoid (399.4 eV), and the quaternary nitrogen (400.8 eV) of PANI.[24–26] These species can also be identified in the corresponding C 1s spectra (Figure S7). Notably, in comparison to GP, the GPM samples all contained a markedly higher atomic percentage of quaternary ammonium, suggesting oxidative interaction of PANI with manganese oxides. The O 1s spectra are shown in Figure 2b, where three major species can be deconvoluted for all samples, C=O (530.90 eV), C_{sp3}–O (531.89 eV), and C_{sp2}–O (533.05 eV).[23] GP contained an additional component at 535.19 eV, indicative of surface-adsorbed water, whereas for the GPM samples, an additional, small peak can be resolved at 530 eV, due to metal-bonded oxygen (M–O). This observation is consistent with the incorporation of manganese oxides in the composites, which accounts for 0.76 atom % for GPM-1 and 0.95 atom % for GPM-2.[27,28]

The Mn 2p spectra are shown in Figure 2c, where two doublets and one satellite can be resolved in the two GPM samples. The first doublet at 640.61/652.67 eV for GPM-1 and 640.40/652.21 eV for GPM-2 can both be attributed to the $2p_{3/2}$ and $2p_{1/2}$ electrons of Mn^{2+}, respectively, suggesting the formation of MnO in the samples.[29] For GPM-1, the second doublet can be resolved at 642.16/653.80 eV and ascribed to the $2p_{3/2}$ and $2p_{1/2}$ electrons of Mn^{4+}, most likely in the form of MnO_2, whereas for GPM-2, the binding energies of the second doublet are somewhat different at 641.62/653.41 eV, consistent with Mn^{3+} in Mn_2O_3.[29] On the basis of the peak areas, one can see that Mn^{2+} is the major species and Mn^{4+} the minor one in GPM-1, whereas Mn^{3+} is dominant in GPM-2 (Table 1).

Bactericidal tests with the nanocomposite materials were then conducted on both Gram-positive and Gram-negative bacteria. Interestingly, the nanocomposites exhibited markedly different antimicrobial activity, despite their similar elemental compositions and average Mn valence state, 2.78 for GPM-1 and 2.75 for GPM-2 (Table 1). Figure 3 depicts the growth curve for Gram-negative *E. coli* conducted under dark conditions and in the presence of varied concentrations of GP, GPM-1, and GMP-2. From Figure 3a, one can see that even at a concentration of 350 mg mL^{-1}, GP did not exhibit any inhibition of *E. coli* growth. For GPM-1 (Figure 3b), at concentrations below 100 μg mL^{-1}, there was virtually no impact on the bacterial growth either with a lag time (t_L) of about 2 h. With a further increase of the GPM-1 concentration, growth of bacteria cells could still be seen; however, t_L increased drastically to 8 h at 200 μg mL^{-1}, 13 h at 250 μg mL^{-1}, and 17 h at 300 μg mL^{-1}, and at a GPM-1 concentration of 350 μg mL^{-1}, bacterial growth was completely inhibited. This indicates that the minimum inhibitory concentration (MIC) of GPM-1 toward *E. coli* is about 350 μg mL^{-1}. Similar behaviors were observed with GPM-2 (Figure 3c), where a somewhat lower MIC was estimated to be 250 μg mL^{-1}. In addition, at the same GPM concentration, increased lag times were observed as compared to those of GPM-1. For instance, at the composite concentration of 200 μg mL^{-1}, t_L is ca. 20 h for GPM-2 as compared to 8 h for GPM-1. Taken together, these results suggest that GPM-2 exhibited a slightly higher inhibition activity toward *E. coli* than GPM-1.

For the Gram-positive bacterium *S. epidermidis*, the overall activity of the nanomaterials was somewhat lower. From Figure S8, one can see that the growth of the bacterial cells was

never inhibited by GP, even at concentrations up to 400 μg mL^{-1}. For GPM-1, there was no inhibition of bacterial growth until the concentration reached 400 μg mL^{-1}, suggesting that the MIC was over 400 μg mL^{-1}. GPM-2 also exhibited a similar MIC, though with a somewhat longer lag time at the same concentration.

Interestingly, photoirradiation markedly enhanced the antimicrobial activity of the GPM nanocomposites with significant differences among the sample types. Figure 4a shows photographs of the LB agar plates after *E. coli* cell suspensions containing different nanomaterials were photoirradiated at 365 nm for up to 20 min. Note that the composite concentration was kept at 60 μg mL^{-1}, which is significantly below the respective MICs determined in the nonphotoirradiated incubation studies (Figure 3). GP and GPM-2 exhibited virtually no inhibition of *E. coli* growth and were similar to the blank control condition. In contrast, GPM-1 nanocomposites demonstrated considerable bactericidal activity upon photo-activation. GPM-1 clearly stood out as the best bactericidal agent, where the CFUs diminished rapidly with prolonged photoirradiation, and after 20 min, essentially no bacterial cells survived. This difference of bacterial inhibition is quantified in Figure 4b, where GMP-1 was 100% effective at inhibiting bacterial growth.

Notably, upon the addition of radical scavengers, such as TBA and EDTA which are specific quenchers for hydroxyl radicals (HO•) and holes (h^+),[30,31] respectively, the photodynamic activity of GPM-1 diminished significantly (Figure 4b). Specifically, in the absence of these scavengers, 5 min photoirradiation reduced the CFUs by 50%. In contrast, the addition of TBA extended the photoirradiation time to 15 min (red dashed curve) and almost 20 min for EDTA (red dotted curve), suggesting contributions from both photogenerated HO• radicals and h^+ to the bactericidal activity.

Similar photodynamic behaviors were observed with *S. epidermidis* (Figure S9), where the GPM samples exhibited markedly enhanced bactericidal activity in comparison to GP and the blank, with GPM-1 being the optimal catalyst. Interestingly, the addition of TBA led to virtually no quenching of the bactericidal activity, whereas a substantially more apparent diminishment was observed with EDTA. This observation suggests that the bactericidal activity arose mostly from oxidative stress by photogenerated holes, likely due to damage of the cell membranes and the impacts on the electron-transport chain within the bacteria.[2]

This is indeed confirmed by EPR measurements. From Figure 5a, one can see that after photoirradiation at 365 nm for 10 min, both GPM samples exhibited a clearly defined 1:2:2:1 hyperfine feature within the range of 3280 to 3340 G at $a_N = a_H = 41.8$ MHz and $g = 2.005$ in comparison to the blank H_2O control. This is characteristic of DMPO–OH adducts, suggesting the formation of HO• radicals.[3,32] In addition, the peak-to-peak intensity can be seen to be markedly greater with GPM-1 than with GPM-2, consistent with the enhanced antimicrobial activity observed above with the former (Figure 4). Interestingly, upon the addition of TBA (Figure 5b), a slight diminishment of the peak-to-peak intensity was observed, and the diminishment became substantially more pronounced with the addition of EDTA (Figure 5c). This observation suggests that HO• radicals were primarily produced by hole oxidation of water, $H_2O + h^+ \rightarrow HO\bullet + H^+$, with a minor contribution from the reduction of oxygen by photogenerated electrons.[33] Note that the formal potential of water

oxidation to HO•, $E°$ = +2.33 V vs normal hydrogen electrode (NHE), is above the valence band edges of MnO (+2.59 V) and MnO_2 (>+3.0 V), where the photogenerated holes reside, but below that of Mn_2O_3 (+1.85 V).[34–36] Since GPM-1 consists of MnO and MnO_2 whereas Mn_2O_3 is the dominant component in GPM-2 (Table 1), HO• production from hole oxidation of water is facilitated by GPM-1 in comparison to GPM-2, as manifested in the photodynamic studies presented above (Figure 4).

The disparity of the photodynamic bactericidal activity of the GPM composites can also be visualized by SEM measurements (Figure 6). In comparison to the intact *E. coli* cell, which exhibited a smooth, rod-like structure (Figure 6a), GPM-2 exhibited minimal impact on the bacterial cell morphology (Figure 6c). However, the addition of GPM-1 led to significant accumulation of the nanocomposites onto the bacterial cell surface, apparent damage to the cell structures, and eventual cell lysis (Figure 6b). Similar behaviors can be seen with *S. epidermidis* (Figure 6d–f).

Taken together, these results suggest that the remarkable loss of cellular integrity of both Gram-positive and Gram-negative bacteria from photoactive GPM-1 can be ascribed to the combined contributions of (i) enhanced adsorption of the nanocomposites onto the cell surfaces and (ii) relatively high contents of Mn^{2+} and Mn^{4+} species in the sample, where the band structures are known to be favorable for water oxidation, a unique feature conducive to the formation of hydroxy radicals, which are potent bactericidal agents.[34–36]

Notably, the GPM nanocomposites also exhibited remarkable stability. Most of the photodynamic studies were carried out within the time span of 2–3 weeks. Yet, rather consistent results were obtained, as manifested in the relatively small error bars in Figures 4 and S9.

4. CONCLUSION

In this study, ternary nanocomposites based on GOQD, PANI, and manganese oxides were found to exhibit apparent antimicrobial activity toward both Gram-negative *E. coli* and Gram-positive *S. epidermidis*. Despite a similar composition and average valence state of Mn, the GPM-1 nanocomposite that contained a high content of Mn^{2+} and Mn^{4+} species was found to exhibit enhanced bactericidal activity under photoirradiation at 365 nm, as compared to the GPM-2 sample with a dominant Mn^{3+} component. Such a disparity of the antimicrobial performance was largely ascribed to the enhanced separation of photoinduced electron–hole pairs in GPM-1 and the unique band structure that was conducive to photocatalytic production of hydroxy radicals via water oxidation by photogenerated holes. Further contribution likely arose from the strong adsorption of the GPM-1 nanocomposites onto the bacterial cell surface. Results from this study highlight the significance of the metal valence state in the manipulation of the nanocomposite photodynamic activity. Such insights are critical in the further design and engineering of effective antimicrobial agents based on functional nanocomposites toward a wide spectrum of bacteria.

Supplementary Material

Refer to Web version on PubMed Central for supplementary material.

ACKNOWLEDGMENTS

This work was supported by the National Science Foundation (CBET-1848841). TEM and XPS studies were carried out at the National Center for Electron Microscopy and Molecular Foundry, Lawrence Berkeley National Laboratory, which is supported by the US Department of Energy, as part of a user project.

REFERENCES

(1). Arias CA; Murray BE Antibiotic-resistant bugs in the 21st century–a clinical super-challenge. N. Engl. J. Med 2009, 360, 439–43. [PubMed: 19179312]

(2). Rojas-Andrade MD; Chata G; Rouholiman D; Liu J; Saltikov C; Chen S Antibacterial mechanisms of graphene-based composite nanomaterials. Nanoscale 2017, 9, 994–1006. [PubMed: 28054094]

(3). Rojas-Andrade MD; Nguyen TA; Mistler WP; Armas J; Lu JE; Roseman G; Hollingsworth WR; Nichols F; Millhauser GL; Ayzner A; Saltikov C; Chen S Antimicrobial Activity of Graphene Oxide Quantum Dots: Impacts of Chemical Reduction. Nanoscale Adv 2020, 2, 1074–1083.

(4). McNamara K; Tofail SAM Nanoparticles in Biomedical Applications. Adv. Phys 2017, 2, 54–88.

(5). Zhang HY; Ji ZX; Xia T; Meng H; Low-Kam C; Liu R; Pokhrel S; Lin SJ; Wang X; Liao YP; Wang MY; Li LJ; Rallo R; Damoiseaux R; Telesca D; Madler L; Cohen Y; Zink JI; Nel AE Use of Metal Oxide Nanoparticle Band Gap To Develop a Predictive Paradigm for Oxidative Stress and Acute Pulmonary Inflammation. ACS Nano 2012, 6, 4349–4368. [PubMed: 22502734]

(6). Liu J; Rojas-Andrade MD; Chata G; Peng Y; Roseman G; Lu JE; Millhauser GL; Saltikov C; Chen S Photo-enhanced antibacterial activity of ZnO/graphene quantum dot nanocomposites. Nanoscale 2018, 10, 158–166.

(7). Liu JL; Shao JZ; Wang YH; Li JQ; Liu H; Wang AQ; Hui AP; Chen SW Antimicrobial Activity of Zinc Oxide-Graphene Quantum Dot Nanocomposites: Enhanced Adsorption on Bacterial Cells by Cationic Capping Polymers. ACS Sustain. Chem. Eng 2019, 7, 16264–16273.

(8). Cao BC; Cao S; Dong PY; Gao J; Wang J High antibacterial activity of ultrafine TiO2/graphene sheets nanocomposites under visible light irradiation. Mater. Lett 2013, 93, 349–352.

(9). Kiani F; Astani NA; Rahighi R; Tayyebi A; Tayebi M; Khezri J; Hashemi E; Rothlisberger U; Simchi A Effect of graphene oxide nanosheets on visible light-assisted antibacterial activity of vertically-aligned copper oxide nanowire arrays. J. Colloid Interface Sci 2018, 521, 119–131. [PubMed: 29558691]

(10). Chiam SL; Pung SY; Yeoh FY Recent developments in MnO2-based photocatalysts for organic dye removal: a review. Environ. Sci. Pollut. Res 2020, 27, 5759–5778.

(11). Saputra E; Muhammad S; Sun HQ; Ang HM; Tade MO; Wang SB Manganese oxides at different oxidation states for heterogeneous activation of peroxymonosulfate for phenol degradation in aqueous solutions. Appl. Catal., B 2013, 142, 729–735.

(12). Ahmed KAM; Peng H; Wu KB; Huang KX Hydrothermal preparation of nanostructured manganese oxides (MnOx) and their electrochemical and photocatalytic properties. Chem. Eng. J 2011, 172, 531–539.

(13). Kamran U; Bhatti HN; Iqbal M; Jamil S; Zahid M Biogenic synthesis, characterization and investigation of photocatalytic and antimicrobial activity of manganese nanoparticles synthesized from Cinnamomum verum bark extract. J. Mol. Struct 2019, 1179, 532–539.

(14). Alimohammadi F; Sharifian Gh. M; Attanayake NH; Thenuwara AC; Gogotsi Y; Anasori B; Strongin DR Antimicrobial Properties of 2D MnO2 and MoS2 Nanomaterials Vertically Aligned on Graphene Materials and Ti3C2MXene. Langmuir 2018, 34, 7192–7200. [PubMed: 29782792]

(15). Haneefa MM; Jayandran M; Balasubramanian V Green Synthesis Characterization and Antimicrobial Activity Evaluation of Manganese Oxide Nanoparticles and Comparative Studies with Salicylalchitosan Functionalized Nanoform. Asian J. Pharm 2017, 11, 65–74.

(16). Wang ST; Dong YH; Cao FJ; Li YT; Zhang ZT; Tang ZL Conversion-Type MnO Nanorods as a Surprisingly Stable Anode Framework for Sodium-Ion Batteries. Adv. Funct. Mater 2020, 30, 2001026.

(17). Gao T; Krumeich F; Nesper R; Fjellvag H; Norby P Microstructures, Surface Properties, and Topotactic Transitions of Manganite Nanorods. Inorg. Chem 2009, 48, 6242–6250. [PubMed: 19462984]

(18). Zeraati AS; Arjmand M; Sundararaj U Silver Nanowire/MnO2 Nanowire Hybrid Polymer Nanocomposites: Materials with High Dielectric Permittivity and Low Dielectric Loss. ACS Appl. Mater. Interfaces 2017, 9, 14328–14336. [PubMed: 28378996]

(19). Luo DC; Zhang GX; Liu JF; Sun XM Evaluation Criteria for Reduced Graphene Oxide. J. Phys. Chem. C 2011, 115, 11327–11335.

(20). Saxena S; Tyson TA; Shukla S; Negusse E; Chen HY; Bai JM Investigation of structural and electronic properties of graphene oxide. Appl. Phys. Lett 2011, 99, 013104.

(21). Zhang JL; Yang HJ; Shen GX; Cheng P; Zhang JY; Guo SW Reduction of graphene oxide via L-ascorbic acid. Chem. Commun 2010, 46, 1112–1114.

(22). Bubb DM; O'Malley SM; Antonacci C; Belmont R; McGill RA; Crimi C Observation of persistent photoconductivity in conducting polyaniline thin films. Appl. Phys. A: Mater. Sci. Process 2005, 81, 119–125.

(23). Li M; Cushing SK; Zhou XJ; Guo SW; Wu NQ Fingerprinting photoluminescence of functional groups in graphene oxide. J. Mater. Chem 2012, 22, 23374–23379.

(24). Patil SH; Gaikwad AP; Sathaye SD; Patil KR To form layer by layer composite film in view of its application as supercapacitor electrode by exploiting the techniques of thin films formation just around the corner. Electrochim. Acta 2018, 265, 556–568.

(25). Ahuja P; Ujjain SK; Arora I; Samim M Hierarchically Grown NiO-Decorated Polyaniline-Reduced Graphene Oxide Composite for Ultrafast Sunlight-Driven Photocatalysis. ACS Omega 2018, 3, 7846–7855. [PubMed: 31458927]

(26). Li YQ; Xia ZB; Gong Q; Liu XH; Yang Y; Chen C; Qian CH Green Synthesis of Free Standing Cellulose/Graphene Oxide/Polyaniline Aerogel Electrode for High-Performance Flexible All-Solid-State Supercapacitors. Nanomaterials 2020, 10, 1546.

(27). Chen S; Shu XX; Wang HS; Zhang JT Thermally driven phase transition of manganese oxide on carbon cloth for enhancing the performance of flexible all-solid-state zinc-air batteries. J. Mater. Chem. A 2019, 7, 19719–19727.

(28). Li XT; Ma JZ; Yang L; He GZ; Zhang CB; Zhang RD; He H Oxygen Vacancies Induced by Transition Metal Doping in gamma-MnO2 for Highly Efficient Ozone Decomposition. Environ. Sci. Technol 2018, 52, 12685–12696. [PubMed: 30346750]

(29). Wagner JM X-Ray Photoelectron Spectroscopy Nova Science Publishers: New York, 2011.

(30). Tan CQ; Wu HT; He H; Lu X; Gao HY; Deng J; Chu WH Anti-inflammatory drugs degradation during LED-UV365 photolysis of free chlorine: roles of reactive oxidative species and formation of disinfection by-products. Water Res 2020, 185, 116252. [PubMed: 32763529]

(31). Grilla E; Petala A; Frontistis Z; Konstantinou IK; Kondarides DI; Mantzavinos D Solar photocatalytic abatement of sulfamethoxazole over Ag3PO4/WO3 composites. Appl. Catal., B 2018, 231, 73–81.

(32). Li JZ; Chen MJ; Cullen DA; Hwang S; Wang MY; Li BY; Liu KX; Karakalos S; Lucero M; Zhang HG; Lei C; Xu H; Sterbinsky GE; Feng ZX; Su D; More KL; Wang GF; Wang ZB; Wu G Atomically dispersed manganese catalysts for oxygen reduction in proton-exchange membrane fuel cells. Nat. Catal 2018, 1, 935–945.

(33). Bartz RR; Piantadosi CA Clinical review: Oxygen as a signaling molecule. Crit Care 2010, 14, 234. [PubMed: 21062512]

(34). Munawar K; Mansoor MA; Basirun WJ; Misran M; Huang NM; Mazhar M Single step fabrication of CuO-MnO-2TiO(2) composite thin films with improved photoelectrochemical response. RSC Adv 2017, 7, 15885–15893.

(35). Saravanan R; Gupta VK; Narayanan V; Stephen A Visible light degradation of textile effluent using novel catalyst ZnO/gamma-Mn2O3. J. Taiwan Inst. Chem. Eng 2014, 45, 1910–1917.

(36). Young MJ; Holder AM; George SM; Musgrave CB Charge Storage in Cation Incorporated alpha-MnO2. Chem. Mater 2015, 27, 1172–1180.

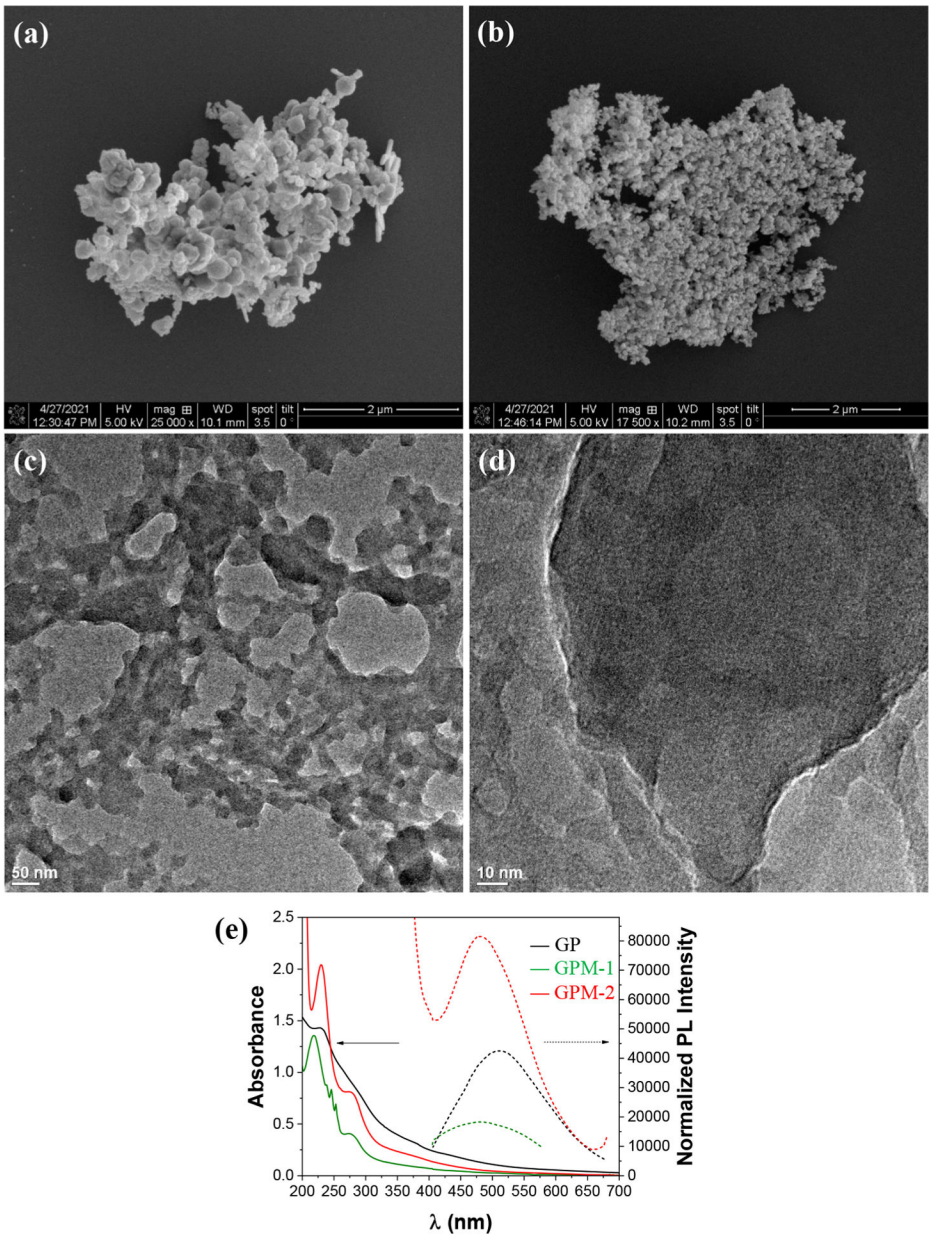

Figure 1.

(a, b) SEM and (c, d) TEM images of (a, c) GPM-1 and (b, d) GPM-2. (e) UV–vis absorption and photoluminescence emission spectra of GP, GPM-1, and GPM-2 nanocomposites.

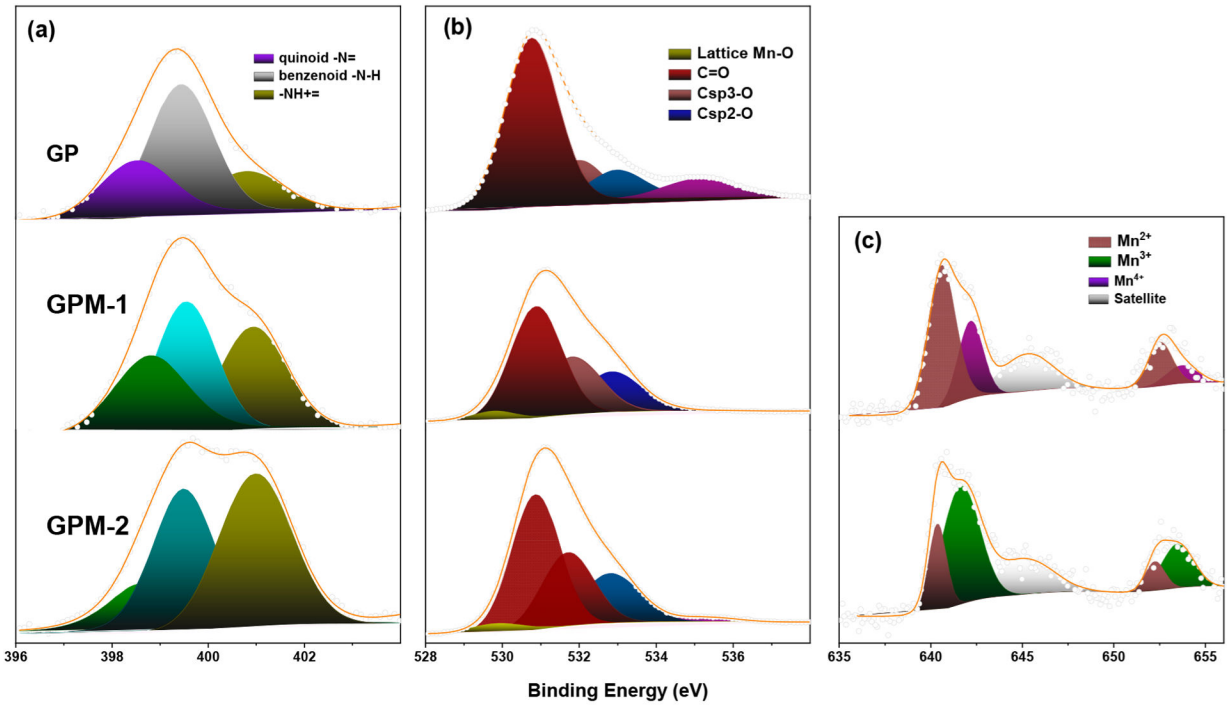

Figure 2.

High-resolution XPS spectra of the (a) N 1s, (b) O 1s, and (c) Mn 2p electrons of the GP, GPM-1, and GPM-2 composites. Dotted curves are experimental data, and shaded peaks are deconvolution fits.

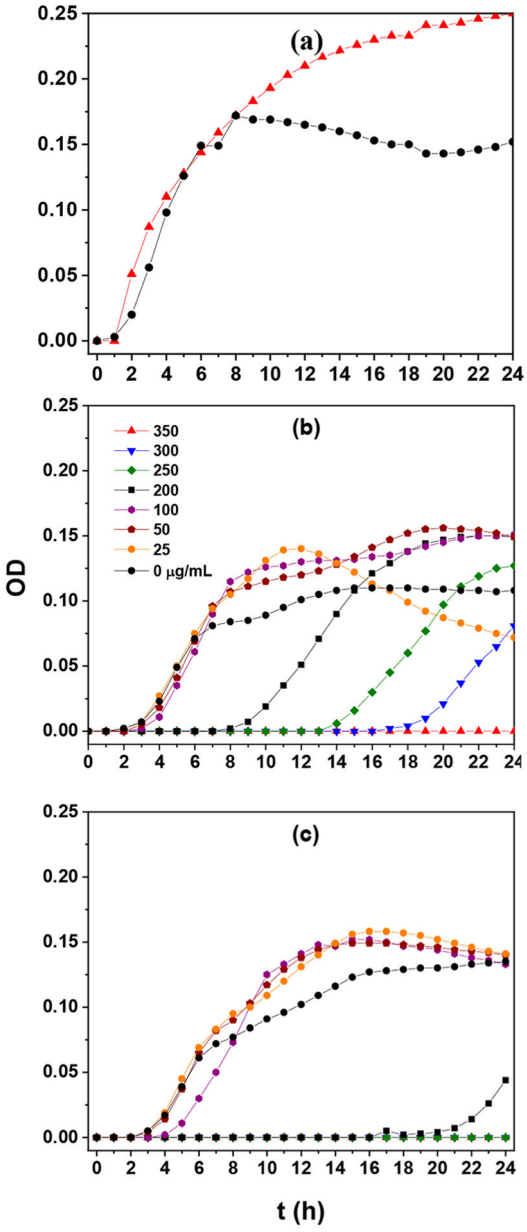

Figure 3.

Growth curves of *E. coli* in the dark with the addition of varied concentrations of (a) GP, (b) GPM-1, and (c) GPM-2.

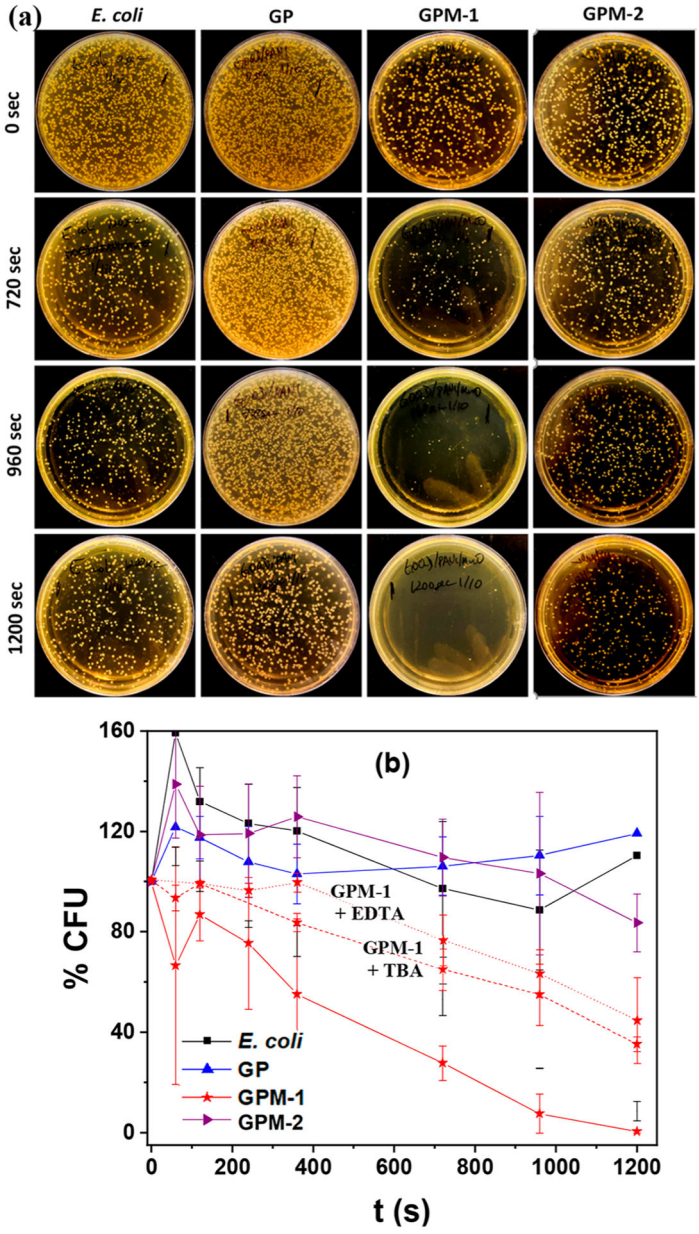

Figure 4.

(a) Photographs of LB agar plates after incubation with *E. coli* cell suspensions under photoirradiation at 365 nm for varied periods of time in the absence and presence of GP, GPM-1, and GPM-2 at a concentration of 60 μg mL^{-1}. (b) Variation of normalized bacteria colony formation units with photoirradiation time from (a), and the corresponding plots in the presence of GPM-1 along with TBA (red dashed curve) and EDTA (red dotted curve) scavengers. Error bars reflect the standard deviations of the triplicate measurements.

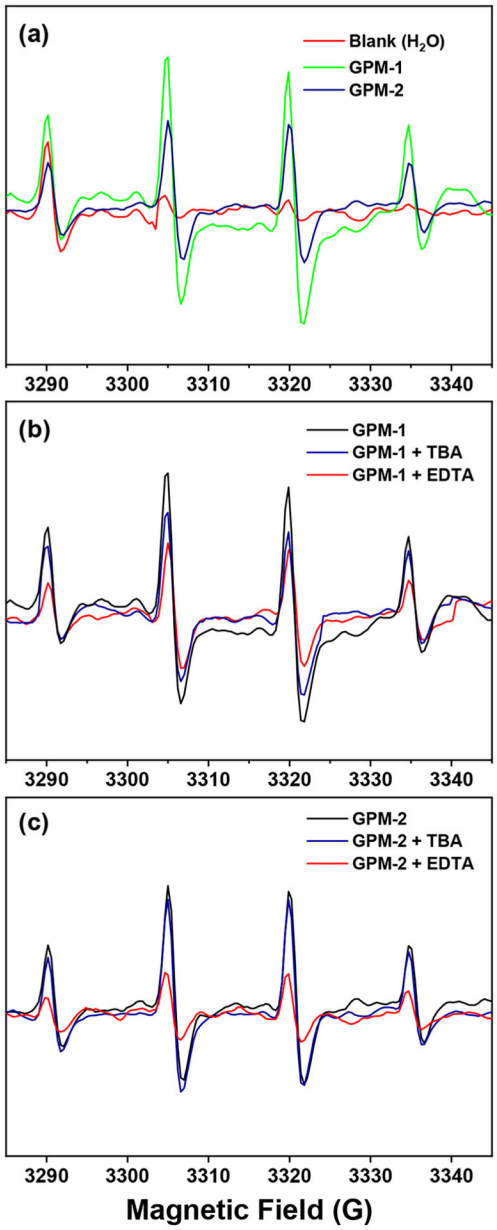

Figure 5.

EPR hyperfine splitting patterns in the presence of DMPO after 10 min of photoirradiation at 365 nm: (a) blank H_2O, GPM-1, and GPM-2; (b) GPM-1 in the absence and presence of TBA and EDTA scavengers; (c) GPM-2 in the absence and presence of TBA and EDTA scavengers.

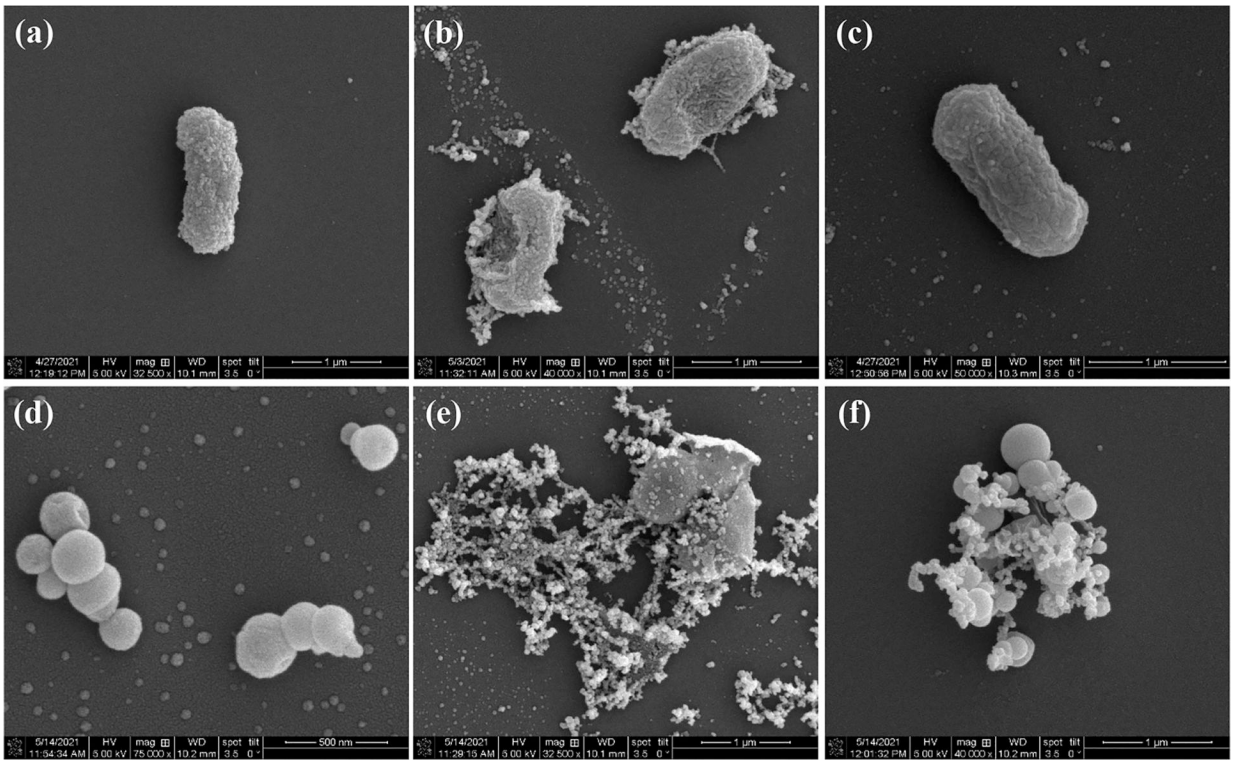

Figure 6.

SEM images of (a–c) *E. coli* and (d–f) *S. epidermidis* in the (a, d) absence and presence of (b, e) GPM-1 and (c, f) GPM-2 nanocomposites after photoirradiation at 365 nm for 15 min.

Table 1.

Elemental Compositions of the Sample Series by XPS Measurements

				Mn (atom %)				
sample	**C (atom %)**	**N (atom %)**	**O (atom %)**	**Mn^{2+}**	**Mn^{3+}**	**Mn^{4+}**	**total Mn**	**average Mn valence state**
GP	64.01	4.07	31.95					
GPM-1	70.38	5.86	23.38	0.246		0.159	0.405	2.78
GPM-2	68.15	5.66	25.81	0.092	0.281		0.373	2.75

ACS Appl Bio Mater. Author manuscript; available in PMC 2022 February 26.